Enhanced durability of carbon nanotube grafted hierarchical ceramic microfiber-reinforced epoxy composites

Enhanced durability of carbon nanotube grafted hierarchical ceramic microfiber-reinforced epoxy composites.

Ajay Krishnamurthy [a,b], Donald L. Hunston [c], Amanda L. Forster [b], Bharath Natarajan [b], Andrew H. Liotta [d,e], Sunny S. Wicks [d], Paul E. Stutzman [c], Brian L. Wardle [d], J. Alexander Liddle [f], Aaron M. Forster [b,*]

a Theiss Research, La Jolla, CA 92037, USA

b Material Measurement Laboratory, National Institute of Standards and Technology, Gaithersburg, MD 20899, USA

c Engineering Laboratory, National Institute of Standards and Technology, Gaithersburg, MD 20899, USA

d necstlab, Department of Aeronautics and Astronautics, Massachusetts Institute of Technology, MA 02139, USA

e Department of Materials Science and Engineering, Massachusetts Institute of Technology, MA 02139, USA

f Center for Nanoscale Science and Technology, National Institute of Standards and Technology, Gaithersburg, MD 20899, USA

Abstract

As carbon nanotube (CNT) infused hybrid composites are increasingly identified as next-generation aerospace materials, it is vital to evaluate their long-term structural performance under aging environments. In this work, the durability of hierarchical, aligned CNT grafted aluminoborosilicate microfiber-epoxy composites (CNT composites) are compared against baseline aluminoborosilicate composites (baseline composites), before and after immersion in water at 25 °C (hydro) and 60 °C (hydrothermal), for extended durations (90 d and 180 d). The addition of CNTs is found to reduce water diffusivities by approximately 1.5 times. The mechanical properties (bending strength and modulus) and the damage sensing capabilities (DC conductivity) of CNT composites remain intact regardless of exposure conditions. The baseline composites show significant loss of strength (44 %) after only 15 d of hydrothermal aging. This loss of mechanical strength is attributed to fiber-polymer interfacial debonding caused by accumulation of water at high temperatures. *In situ* acoustic and DC electrical measurements of hydrothermally aged CNT composites identify extensive stress-relieving micro-cracking and crack deflections that are absent in the aged baseline composites. These observations are supported by SEM images of the failed composite cross-sections that highlight secondary matrix toughening

* Corresponding author. Tel: 301-975-8701. E-mail: aaron.forster@nist.gov (Aaron Forster)

mechanisms in the form of CNT pullouts and fractures which enhance the service life of composites and maintain their properties under accelerated aging environments.

1. Introduction

Fiber reinforced plastics (FRPs) are used extensively in aerospace, automotive, and energy applications due to their high stiffness and strength-to-weight ratios, as well as their ability to be manufactured into complex shapes [1] - [4]. Traditionally, FRPs are anisotropic materials that are strong in the fiber plane with relatively weak interlaminar regions that are susceptible to failure when subjected to non-tensile loading conditions such as shear or compression [5], [6]. Composite engineers have addressed the inadequacies in the interlaminar region by using three-dimensional fiber architectures such as weaving, stitching, braiding or z-pinning, which add fiber yarn reinforcements between adjacent fiber layers to improve structural properties under shear and compressive loading. However, these fiber additions lead to a significant decrease in the composite strength due to the geometric defects introduced by fiber crimping, fracture and distortion, while increasing the potential for weak, resin-rich regions [7], [8]. The optimization of mechanical properties continues to require specialized composite designs and remains a primary area of focus for this field. Common aerospace-grade epoxy matrices are non-conductive and exhibit poor functionality toward electrostatic discharges, electromagnetic interference and lightning strike protection. Hence, secondary challenges for aerospace applications are mitigation of static discharge and the use of non-destructive techniques for sensing hidden damage within a composite structure.

Highly conductive, mechanically superior nanofillers such as CNTs can address deficiencies in mechanical (non-tensile) and electrical properties of aerospace composites [9] - [12]. Even at low volume fractions, the CNT networks stiffen the polymer matrix and prevent rapid crack growth through secondary energy dissipation mechanisms such as CNT pullouts and CNT fractures, that can enhance the service life of nanotube enabled composites [13]. CNTs are impregnated into fiber composites using two principal methods: matrix dispersion and fiber attachment. Matrix dispersion involves directly dispersing CNTs in the resin followed by resin infusion into fiber layers, whereas fiber attachment consists of directly adhering the CNTs onto fiber layers prior to resin infusion. Literature studies indicate that the increase in mechanical performance of a nanocomposite is a strong function of resin/nanofiller interfacial properties for a given CNT aspect ratio and dispersion

[14] - [17]. As FRPs manufactured by matrix dispersion often encounter CNT agglomeration with no significant improvement in mechanical properties, [18] - [20] the current study will focus on FRPs manufactured by directly adhering CNTs to fiber surfaces.

Multi-walled carbon nanotubes (MWCNTs) are grown on top of the alumina microfiber surface *via* a chemical vapor deposition (CVD) process that results in a dense "mohawk" CNT forest extending from the fibers. The resulting "fuzzy" fiber textile layers are then stacked and infused with a thermoset resin using commercial resin transfer manufacturing techniques. Improvements in both interlaminar and intralaminar properties are observed in these hybrid systems, where the radially arranged CNTs wick the polymer resin via capillary action to form strong interfacial bonds between the resin and the nanotubes [21], [22]. In addition, CVD growth of the CNTs increases the spacing between individual fibers and increases the area of the tow cross-section. This results in a lower volume fraction of resin pockets between fiber tows and textile layers with CNTs bridging the inter- and intra-ply regions within the composite [23]. Even at a low CNT volume fraction (approximately 1 % by volume), the electrical conductivity of composites can be improved by up to 6 orders of magnitude [24].

Aerospace applications of nanoengineered composites rely on their shear strength and toughness (joints and wing spans, landing gear trailing arms), electrical conductivity (de-icing, EMI shielding) and thermal properties (engine exhausts and nozzles), where these materials are expected to perform for long operating periods at varying temperature, strain, and humidity conditions [25] - [29]. Optimizing the microstructure of the CNT network and the interfacial interactions to tailor the composite for these important applications requires novel approaches for manufacturing and design. One area lacking data for hybrid FRPs is durability. This information is critical to avoid a material system with poor service lifetimes. The established methodologies for characterizing FRP aging are exposure to "hot and wet" conditions followed by mechanical testing and Highly Accelerated Lifetime Testing (HALT), which provides a pass/fail condition, but only has a limited capacity to predict product reliability [30], [31]. This work utilizes accelerated aging protocols and *in situ* experimental measurements to identify and track the evolution of failure mechanisms in these advanced composites.

Several routes have been identified through which composites degrade under hydrothermal conditions. At short exposure times or low temperatures, plasticization of the matrix and swelling

induced interfacial stresses lead to reduced mechanical performance. These effects however, may be reversed upon drying [32] - [34]. At longer exposures or high temperatures, resin and fiber degradation, and void formation, cause irreversible reduction in the mechanical performance through a combination of failure modes that include fiber damage, matrix cracking or interface debonding [35] - [42]. The presence of MWCNTs in composites has the potential to affect composite durability by modifying water absorption, resin cure chemistry and interfacial bonding characteristics. The conclusions of the majority of early studies on dispersed CNT systems differ depending on the CNT functionalization, CNT volume fractions, dispersion methodology and the CNT/polymer interactions. Some of the prominent studies on durability of these systems are summarized in references [43] - [47].

While there are several studies on the long-term effects of water and temperature on resin chemistry and mechanical property changes in dispersed CNT-epoxy and CNT-FRP systems [43] - [47], there are no studies on the durability of hierarchical composites, where the CNTs are directly attached to fiber surfaces. The current study focuses on measuring the aging characteristics (water diffusivity, polymer plasticization and hydrolysis reactions) of the nanoscale CNT reinforcement of the polymer in a model aluminoborosilicate fiber composite system. The aluminoborosilicate fibers used here are heat treated and suitable for high-temperature refractory applications. It has been previously shown that the CVD growth process degrades commercial fiber materials such as glass or carbon [48], thereby making them unsuitable for studying the properties of grafted CNT fiber-composites. Though there have been recent advancements in depositing carbon nanotubes onto individual carbon fiber tows, obtaining a complete 3-D CNT coverage on fiber-mats using the CVD process is still a challenge [49]. Both these requirements are well satisfied in the case of aluminoborosilicate fibers, which can withstand the harsh growth conditions encountered during the CVD process and support 3-D CNT growth [26]. These fibers have been previously used to understand several aspects of the hierarchical CNT composites including manufacture and processing ([23], [50]), physical properties ([21], [24], [25], and [28]), and resin infusion. Hence, despite having lower mechanical properties than commercially relevant fibers (glass and carbon), this aluminoborosilicate fiber system is useful for investigating the aging characteristics of the hierarchical CNT composites.

Various physical and chemical characterization techniques were employed to study the aging characteristics of the CNT composites. The effect of CNTs on water absorption and solvent diffusivity into the resin, was studied by gravimetric water uptake measurements. Combining mechanical strength measurements with *in situ* acoustic and electrical measurements, the changes in damage propagation were studied as a function of mechanical strain and successfully correlated against SEM images of failed surfaces. Finally, the primary cause of strength failure in hydrothermally aged alumina fiber specimens was determined using SEM, Fourier transform infrared spectroscopy-attenuated total reflectance (FTIR-ATR), and differential scanning calorimetry (DSC). Our results demonstrate that the presence of radially grown CNTs helps mitigate interfacial failures in fiber reinforced composites under accelerated aging environments and, furthermore, provides a significant increase in the component lifetime.

2. Materials and Methods

2.1.Composite manufacture

The laminates used in the study consist of plain weave aluminoborosilicate fiber mats (approximately 55 % by mass, with or without CNTs) (ultra temp 391 fibers, Cotronics Corporation, NJ, areal density of 371 g/m^2) that are infiltrated with an aerospace epoxy resin (RTM6, Hexcel Corporation) using a Vacuum Assisted Resin Infusion (VARI) process [25]. The as-received fibers were treated with a non-hygroscopic coating/sizing by the manufacturer. MWCNTs (approximately 2 % by mass) were deposited on fiber surfaces using a CVD process with ethylene as the carbon precursor [49]. The fiber cloth is dipped in a 50 mM solution of iron nitrate in iso-propanol and dried in an oven for 8 h at 30 °C. The cloth is then cut into approximately 50 mm by 178 mm plies and inserted into the CVD furnace where it is heated to 650 °C under 1040 sccm of hydrogen for 5 mins. The fibers are then introduced to ethylene gas at 350 sccm for 3 mins to deposit aligned MWCNTs that are approximately 19 μm long. Additional details of MWCNT growth and composite manufacture have been discussed elsewhere [23], [25], [50], [51]. Prior to resin infusion, the fiber stack is kept at about 150 °C for approximately two hours under vacuum conditions (740 mm Hg) to remove any residual moisture content. The RTM6 epoxy resin is then degassed at around 80 °C and is introduced in a controlled fashion into the laminate at approximately 90 °C [25]. The composite is then cured at about 160 °C and post cured at 180 °C. The density of the cured baseline and CNT composites, measured using helium

pycnometry were found to be ((1.58 ± 0.01) g/cm^3) and ((1.61 ± 0.01) g/cm^3) respectively. These values are in agreement with those determined using direct mass and dimensional measurements on the composites, indicating minimal void content. The void content on these composite specimens as estimated from previous study by Wicks et al. is less than 2 % by volume [21], [28]. An illustration of the hierarchical CNT composite has been presented in Fig. 1.

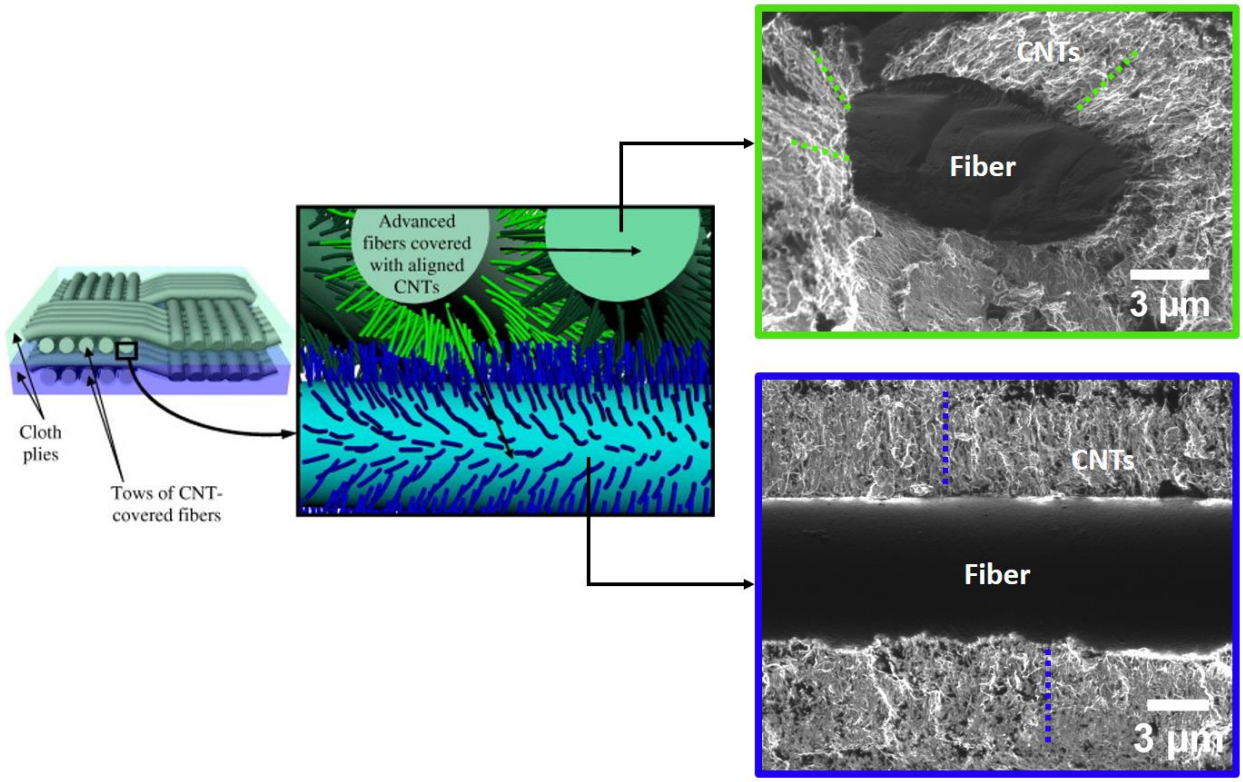

Figure 1: A CNT composite showing the woven Al_2O_3 microfiber with CNTs inside the polymer matrix in illustration (*left*) and SEM images of the CNT alignment on the fiber surfaces within the composite (*right*). The green and blue dotted lines denote radial alignment of MWCNTs from the fiber surface based on fiber orientation.

2.2.Exposure protocols

A tile saw cooled with water, was used to machine the sample length and width. The cut sides of the samples were wet polished in the following order: 600, 800, 1200 and finally 2000 grit silicon

carbide paper. Two different sample lengths were used for flexure testing and short span testing. The length of flexure specimens was approximately 52 mm. The length of the short span specimens was approximately 17 mm. The deviation in the length, within each specimen, was less than ± 0.1 mm. The width for all the specimens was approximately 4.25 mm. The deviation in the width, within each specimen was less than ± 0.2 mm (as per ASTM 79 [52]) for over 90 % of the specimens tested. The thickness of all specimens was approximately 2.35 mm and within the tolerance limits of ± 0.2 mm (as per ASTM 790 [52]) for each specimen. Three exposure conditions namely, Hydro (Hy) (nominally 25 °C, t_{max} = 180 d), Hydrothermal short (HT-S) (nominally 60 °C, t_{max} = 15 d) and Hydrothermal long (HT-L) (nominally 60 °C, t_{max} = 90 d) were chosen. The samples were sealed in a glass jar filled with deionized water using a rubber stopper wrapped in polytetrafluoroethylene (PTFE) film prior to application of the above-mentioned temperature exposures. The exposed samples were compared against control specimens (Ctrl) that were stored at room temperature in air. During the exposure period (t_{max}), the samples were removed periodically from the glass jars, thoroughly wiped to remove excess water, and weighed using a balance of ± 0.01 mg resolution before being placed back into the jar. The Hy, the HT-L, and the HT-S exposures were conducted using a sample population of n = 6, n = 5, and n = 4 specimens, respectively. At the end of the exposure period, the samples were removed from the water and kept under desiccating conditions inside a bell jar filled with anhydrous calcium sulfate. They were maintained under these conditions until the mean specimen mass was nominally within ± 0.05 % of its original value.

2.3.Mass uptake water:

The mass gain, M_e (%), measured as a function of exposure time is calculated as per Eqn. 1 given below,

$$M_e(\%) = \frac{M_t - M_i}{M_i} \times 100 \quad (1)$$

where M_t is the mass of the composite at exposure time t, and M_i is the initial mass of the composite before exposure.

2.4.Mechanical characterization

The 3-point bend test (ASTM D790 [52]) was used to characterize the strength and the bending modulus of composite materials. The term apparent flexure strength is used in place of flexure strength for the flexure specimens, and breaking strength in the case of short span specimens, due to the non-conformity of the specimen widths and spans to the ASTM D790 [52] standard. Further, the breaking stresses for the short-specimens have been included to qualitatively compare the reduction in breaking strength changes observed in flexure and the short specimens (different span to depth ratio) for both composite types. All the tests were conducted using a 5 kN load cell, on an electromechanical, universal test frame at ASTM prescribed loading rates. The mechanical testing was often coupled with *in situ* acoustic and electrical measurements mentioned below. An illustration of the entire test set-up has been provided in Fig. S1.

2.5.Acoustic testing

Acoustic testing was conducted using a commercially available acoustic emission system with a preamplifier to power an acoustic sensor (analog bandwidth of 50 kHz to 400 kHz) at a resonant frequency of about 150 kHz. The sensor was placed on the top loading anvil of the 3-point bend apparatus and was acoustically coupled to the surface using vacuum grease. All experiments were conducted at a pre-amplification of about 20 dB with a 40 dB threshold limit to eliminate background noise interference. Calibrations of the system were conducted using ASTM E976 [53] to confirm the repeatability of the sensor and to determine the pre-amplification levels required for the measurement.

2.6.Electrical characterization

The DC electrical conductivity was measured using a two-probe technique (Fig. S1, Fig. S2, and Fig. S3). Contact pads (approximately 5 mm long) were placed at both ends of the composite and were generated by a three-step process. First, a nominal 5 nm chromium coating was sputter deposited. Then, a nominal 100 nm gold film was sputter deposited on the chromium layer at pressures close to 0.1 Pa. The chromium coating was used to promote adhesion between the gold film and the composite surface. Finally, a thin coating of silver paste was applied onto the gold surface (Fig. S1). Silver-coated copper wires (approximately 1.11 mm OD) were adhered to the contact pads for conducting the electrical measurements.

The circuit diagram for the electrical measurement is provided in Fig. S2. The specimen is attached in series with a 1.5 kΩ resistor to prevent damage from excessive current flow. A DC voltage of about 7 V was applied across the circuit and the corresponding voltage drop across the specimen was recorded continuously using a digital multimeter interfaced to a computer. The circuit current was monitored using a handheld multi-meter and the resistance change was computed as a function of the voltage change. Prior to the mechanical testing, a current-voltage (I-V) curve was generated by sweeping the voltage between 1 V and 10 V. The I-V curves (not shown) exhibit linear behavior with no hysteresis within this range. The sample resistivity (Ω-cm) calculated for the CNT Ctrl, CNT Hy and CNT HT-S specimens using the 2-probe method are (17.43 ± 6.57), (30.38 ± 6.38), and (23.94 ± 8.96), respectively. It is noted that the reported resistivity values are not absolute as they have not been corrected for the various contact resistances involved during the two-probe measurement. In the context of this manuscript, resistivity is used as a qualitative metric to compare damage accumulation during the bending of aged and unaged CNT specimens.

2.7.Thermal Properties

Changes in glass transition temperature (T_g) of the epoxy resin inside the composite samples were monitored by conducting DSC measurements on thin specimens (< 500 μm in thickness), machined close to the failure surfaces using a low speed sectioning saw (region of interest shown in Fig. S3b). At least two replicates were used per exposure condition for each sample type with masses ranging between 6 mg and 10 mg. The specimens were sealed in a hermetic aluminum sample pan and cycled 4 times (2 heating and 2 cooling cycles) between 30 °C and 250 °C at a ramp rate of approximately 5 °C/min. The T_g was then determined from the onset of the endotherm (intersection tangents) of the first heating cycle to understand the effect of the environmental exposure on the polymer chemistry.

The degradation characteristics and the individual component mass fractions of the composite were evaluated in air by undertaking mass-loss measurements in a thermogravimetric analyzer (TGA) (region of interest shown in Fig. S3b). Two samples for each condition, weighing between 8 mg and 12 mg, were heated to approximately 500 °C at the rate of nominally 20 °C/min, where they were isothermally maintained for about 25 min. The samples were then further heated to approximately 800 °C at a rate of nominally 20 °C/min and isothermally maintained for about 25

min to completely burn off any remaining organic content. The fiber mass fraction percentages were then estimated from the residual alumina fiber mass.

2.8.Chemical Analysis

FTIR-ATR was used to monitor chemical changes occurring in the polymer resin. Sectioned composite samples were analyzed on a spectrometer equipped with a liquid nitrogen-cooled mercury cadmium telluride (MCT) detector (region of interest shown in Fig. S3b). The applied pressure was maintained consistent across specimens using the LED indicator on the front of the ATR accessory, and 256 individual scans were collected at a resolution of nominally 4 cm^{-1} between 650 cm^{-1} and 4000 cm^{-1}. The spectral baseline manipulation was carried out by subtracting baseline curves created using a commercially available software. For each exposure condition, 4 individual spectra were collected and normalized against the 1514 cm^{-1} peak corresponding to the C-C stretching vibration of the aromatic ring [54]. The effect of oxidation in the amine peaks were characterized by averaging the spectral intensities at 3398 cm^{-1}. Typical standard uncertainties for spectra measurement are ± 4 cm^{-1} in wavenumber and ± 1 % in peak intensity.

2.9.SEM

Microstructure analysis was carried out on polished side surfaces (region of interest shown in Fig. S3a) and failed cross-sections (region of interest shown in Fig. S3b) of the composite specimens using an incident electron beam energy of 2 kV to 5 kV and 0.1 nA to 0.2 nA probe current. The alumina samples were viewed under the SEM after sputter coating them with 3 nm to 5 nm of gold. All SEM imaging was conducted on a dual beam FIB. High contrast images were generated to highlight the crack structure by processing the images on ImageJ software [55].

3. Results and Discussion

Understanding the aging process and its effect on the performance of FRPs requires a thorough experimental methodology. First, we address whether the presence of a small volume-percent of CNTs can affect the water diffusion which eventually influences the rate of chemical changes in a fiber-resin system. Next, a unique combination of *in situ* acoustic and electrical measurements are used with post-fracture SEM images to present the physics of flexure failure as a function of aging environment. Finally, we use thermal analysis, chemical spectroscopy, X-ray diffraction, and SEM

imaging to identify the potential for polymer and fiber degradation, and to support the hypothesis of fiber/polymer interfacial failure.

3.1.Water uptake

The water uptake of the flexure specimens is shown in Fig. 2. The mass fraction of water absorbed at Hy conditions after about six months was (0.92 ± 0.04) % and (0.75 ± 0.04) % for baseline and CNT composites, respectively (Fig. 2a). This increased to (1.18 ± 0.04) % for baseline composites and (0.98 ± 0.11) % for CNT composites, in roughly half the exposure time at HT-L conditions (Fig. 2b). As the fiber mass fraction across the test specimens was similar (54.56 ± 1.45) % (Table 1), the differences in the water absorption percentages between the baseline and CNT composites is attributed to the presence of 1 % by volume (≈ 2 % by mass) CNTs which reduce the overall resin content. Assuming all the water to be completely absorbed by the resin with a minimal void content, the normalized (resin mass fraction based), near-equilibrium water content percentages at HT-L conditions was calculated to be (2.59 ± 0.64) % for the baseline composites and (2.27 ± 0.80) % for the CNT composites. This is in agreement with the observations of a previous study, where the RTM6 resin was found to absorb around 2.23 % of its mass by water, under similar exposure conditions [56] (calculations in supporting info. Table S1 and Fig. S4).

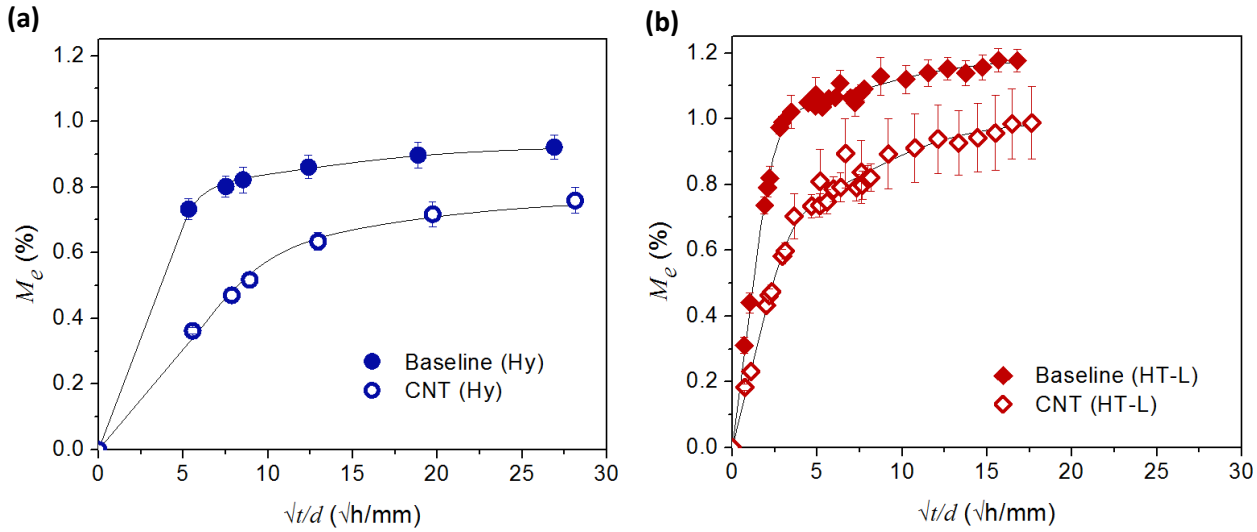

Figure 2: Water absorption in composite specimens at long term exposure conditions: (a) Hy (*left*) and (b) HT-L (*right*). Mass gain, M_e (%) is represented as a function (√*t/d*) (thickness normalized time scale) to enable easy comparison against the Fickian diffusion model which predicts a linear dependence of M_e % vs (√*t/d*) at initial stages of water diffusion. The error

bars on the plots represent one standard deviation of the mean of *M* for each sample population (*n* = 6 for the Hy exposure (25 °C, 180 d) and *n* = 4 for the HT-L exposure (60 °C, 90 d)).

Table 1: Residual fiber mass percentages in the composite specimens obtained from the TGA (region of interest shown in Fig. S3b). The uncertainties represent one standard deviation of the mean alumina fiber mass (*n* = 2) in the composite for each condition.

Fiber mass percentages (%)		
Exposure condition	Baseline composite	CNT composite
Ctrl	54.05 ± 0.71	56.57 ± 2.19
Hy (25 °C, 180 d)	53.03 ± 0.84	55.39 ± 3.06
HT-S (60 °C, 15 d)	52.83 ± 0.55	53.39 ± 0.33
HT-L (60 °C, 90 d)	51.90 ± 0.52	59.36 ± 1.07
Mean	52.95 ± 0.96	56.18 ± 2.74

Water diffusivity inside a composite can be Fickian or non-Fickian in nature. The Fickian diffusion model assumes a linear dependence of simulated mass gain (M_s %) vs $\sqrt{t/d}$ initially, followed by an asymptotical equilibrium attained over long exposure times [44]. From Fig. 2, it is evident that the water uptake at both long-term exposures follow a Fickian trend at early stages, but do not attain complete saturation within the time frame of experimentation, similar to what was reported by Simar et al. [56] at 35 °C and 70 °C exposure conditions. This pseudo-Fickian behavior was therefore characterized using the Langmuir diffusion model (non-Fickian) that assumes water inside composites to exist in two phases, namely, the free state where the water molecules are free to diffuse inside the matrix, and the bound state where the water molecules are combined physically or chemically within the matrix [57].

The absorption data for each composite type and exposure condition, normalized against near-equilibrium water content and overlaid against the Langmuir fit is presented in Fig. 3. The steeper slope in the linear section of the sorption curves denotes faster initial water diffusivities for baseline composites, compared to the CNT composites. Further, it is evident that the water diffusivity is a strong function of the exposure temperature, where the composites subjected to high temperature exposure show faster diffusivities than their room temperature counterparts. This is confirmed by the diffusion coefficients calculated using the Langmuir absorption model (Eqn. 2 [57]). Water diffusivities in hydrothermally exposed baseline and CNT composites are roughly

68 and 58 times higher than the Hy specimens, with the CNT composites showing about 1.4 and 1.6 times slower water diffusivities than the baseline composites during these exposures (Hy and HT-L) (Table 2). Such reductions in water diffusivity have been observed in prior studies on dispersed CNT systems, where the CNT networks are found to hinder water diffusion by providing circuitous pathways for water transport. [43], [44], [58]. The diffusion coefficients obtained in this study are similar to those reported previously for a neat RTM6 resin, ≈ 56 x 10^{-9} cm^2/s under hydrothermal conditions (70 °C, water) and ≈ 8 x 10^{-9} cm^2/s at room temperature conditions (35 °C, 90 % R.H) [55]. Though the CNT composites show lower diffusivities than the baseline composites at both exposure temperatures, the activation energies for solvent diffusion remain similar in both specimens, approximately 99.45 kJ/mol (23.77 kcal/mol) for the baseline composites and 95.69 kJ/mol (22.87 kcal/mol) for the CNT composites.

$$M_s\% = M_m\% \left[1 - \frac{\alpha}{\alpha+\beta} e^{-(\alpha t)} - \frac{\alpha}{\alpha+\beta} - \frac{8}{\pi} e^{-\left(\frac{Dt}{d^2}\pi^2\right)} \right] \quad (2)$$

where M_s % is the simulated mass gain as a function of exposure time, M_m % is the mass gain of the composite at saturation, α is the probability of a water molecule to move from a combined to a free phase, β is the probability of a water molecule moving from a free phase to a combined phase, D is the diffusion coefficient (cm^2/s), and d is the thickness of the sample (cm).

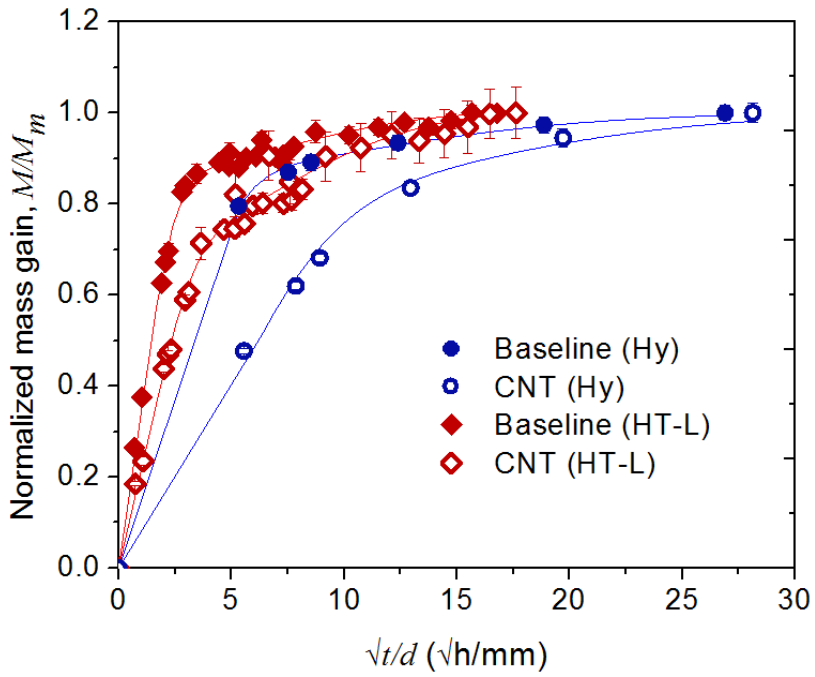

Figure 3: Consolidated water sorption in composite specimens at long term exposures normalized against their equilibrium water content. The symbols represent the experimental data (M_e/M_m) and the lines represent the Langmuir model fit (M_s/M_m). The error bars represent the standard error on one standard deviation of the mean for M_e/M_m in each sample population at Hy (25 °C, 180 d), and HT-L (60 °C, 90 d) conditions.

Table 2: Water diffusivity into flexure specimens exposed to hydro and hydrothermal conditions, respectively. The uncertainties are derived from the least squares fit of the Langmuir model with χ^2 values of 98 % and above.

Diffusion coefficient, D (10^{-9} cm^2/s)		
Exposure condition	Baseline composite	CNT composite
Hy (25 °C, 180 d)	1.3 ± 0.5	0.9 ± 0.5
HT-L (60 °C, 90 d)	85.1 ± 9.0	52.8 ± 1.4

3.2.Mechanical Testing

The mechanical properties of desiccated composite specimens are shown in Fig. 4. The flexure specimens used in the 3-point bend test have a span-to-depth (L/d) ratio of 16:1 as per ASTM D790 [52] to induce fiber dominated bending failures. The short specimens (L/d of 4:1) were used to

induce interlaminar failures, as per ASTM D2344 [59]. However, due to low fiber mass fractions (53 % to 55 %) and low bare fiber strength (tensile strength of approximately 1724 MPa, as per manufacturer specifications [60]), a shear dominated failure was not observed in the woven fiber composites with shorter lengths. Further, from Fig S5, it is observed that the short specimens predominantly fail due to large tensile forces acting through the depth of the laminate, similar to the flexure specimens. Therefore, the stress (σ) in flexure and short specimens were calculated using the bending equation shown in Eqn. 3 (ASTM D790[52]) and termed as apparent flexure strength (σ_{fs}) and breaking strength (σ_{bs}), at sample failure.

$$\sigma = \frac{3PL}{2bd^2} \tag{3}$$

where σ is the stress in the midpoint (MPa), P is the applied force at a given point on the load deflection curve (N), L is the support span (mm), b is the specimen width (mm), and d is the specimen thickness (mm).

The strain (ε) experienced by flexure specimens as a function of loading conditions were calculated using Eqn. 4 (ASTM D790) [52]and termed as strain to failure (ε_f) at sample failure.

$$\varepsilon = \frac{6Td}{L^2} \tag{4}$$

where ε is the strain in the other surface (mm/mm), T is the maximum deflection at the center of the beam (mm), L is the support span (mm), and d is the specimen thickness (mm).

The apparent flexure strengths of the flexure specimens prior to exposure were estimated to be (224 ± 15) MPa and (188 ± 23) MPa for baseline (Ctrl) and CNT (Ctrl) composites (Fig. 4a and 4b). These are well in agreement with values reported previously by Wicks et al. [51]. After a long hydrothermal exposure (HT-L, 90 d), the strength properties of the baseline composites were found to decrease by approximately 44 %, a trend which was consistent across both flexure (Fig. 4a) and short (Fig. 4c) specimen dimensions. Similar strength reductions were observed in the baseline composites even after the short term (15 d) hydrothermal exposure (HT-S). To understand the role of temperature and exposure period on the degradation kinetics of the baseline specimens, both composite types (baseline and CNT) were subjected to a long-term, room-temperature exposure

(Hy), where, even after a six-month duration, no strength reductions were observed in either composite type (Fig. 4a and 4b). Therefore, it is evident that the degradation mechanism becomes active only at higher temperatures in the presence water. A minimum solvent concentration for failure was not determined, but the strength reductions in the baseline composites were found to occur even at sub-equilibrium water content (≈ 1 %), at high temperatures. Though the baseline composites undergo a significant loss in the apparent flexure strength, they show no decline in their bending moduli (E) (Eqn. 5) after any environmental exposure, which indicates the absence of extensive fiber or polymer degradation in these systems [42] (Table 3).

$$E = \frac{(\sigma_2 - \sigma_1)}{(\varepsilon_2 - \varepsilon_1)} \tag{5}$$

where E is the bending modulus (chord modulus) (GPa), σ_2 and σ_1 are the flexural stresses (MPa) calculated from Eqn. 3 at predefined points on the load deflection curve, and ε_2 and ε_1 are the flexural strains (mm/mm) corresponding to the stress values, calculated using Eqn. 4

When compared to the baseline composites, the CNT composites were found to exhibit invariant mechanical properties (strength and modulus) under all exposure conditions. As shown in Fig. 4b, the deviations in apparent flexure strength and strain at failure for the CNT samples remain well within the error bars for the measurements. This highlights the effectiveness of CNT reinforcements in maintaining structural integrity of composites under accelerated aging conditions, by mechanisms such as CNT pullouts and CNT fractures, as identified in previous studies [13], [21].

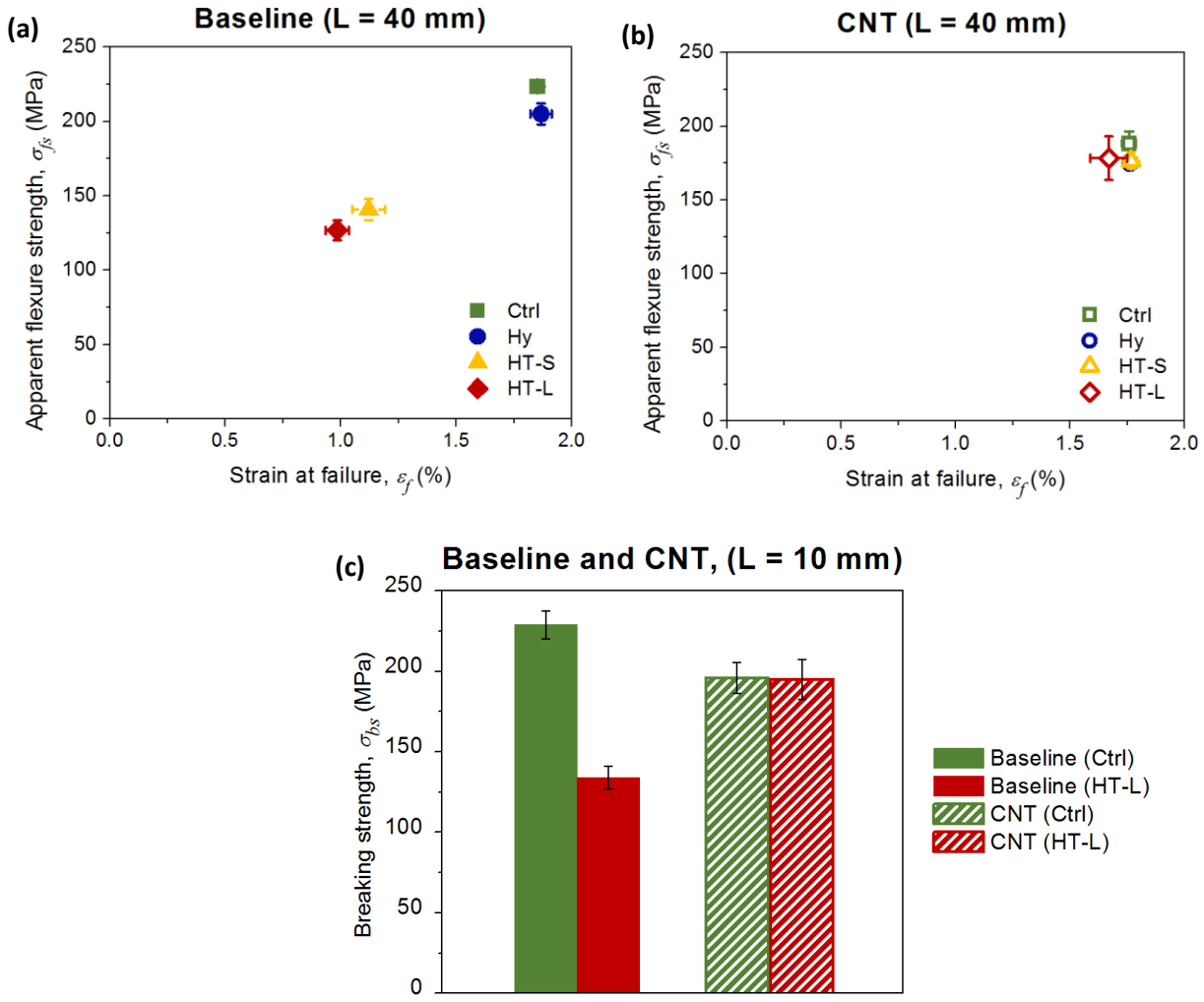

Figure 4: The apparent flexure strength (σ_{fs}) versus strain at failure (ε_f) for flexure specimens (span, L = 40 mm) after Ctrl, Hy (25 °C, 180 d), HT-S (60 °C, 15 d), and HT-L (60 °C, 90 d) exposures in (a) baseline and (b) CNT composites, and (c) Breaking strength (σ_{bs}) of short specimens (span, L = 10 mm), after 90-day hydrothermal exposure, HT-L (60 °C, 90 d). The error bars for the flexure specimens represent the standard error on one standard deviation of the mean apparent flexure strength for each specimen population at the indicated exposure time t_{max}. The error bars for the short specimens represent the standard error on one standard deviation of the mean breaking strength at t_{max}.

Table 3: Bending modulus (chord modulus) of the fiber composite specimens represented according to exposure condition. The uncertainties represent the standard deviation of the bending modulus for each specimen population calculated at t_{max}.

Bending Modulus, *E* (GPa)		
Exposure condition	Baseline composite	CNT composite
Ctrl	13.49 ± 0.72	12.05 ± 0.87
Hy (25 °C, 180 d)	12.01 ± 0.84	11.06 ± 0.66
HT-S (60 °C, 15 d)	13.36 ± 0.36	11.51 ± 1.10
HT-L (60 °C, 90 d)	13.64 ± 0.58	12.42 ± 2.25

Although flexure testing provides insight into the bending modulus and strength magnitude changes in FRPs, the presence of CNTs leads to *different* failure mechanisms for similar loading conditions. A study on the failure mechanisms of the composites was carried out, *in situ*, using two different techniques. The excellent electrical conductivity of MWCNTs has been previously utilized to sense damage in FRPs [61], where disruptions in CNT network tube-tube contacts may be correlated to strain-induced damage occurring in the bulk of the composites. This technique, however, cannot be extended to study the non-conductive baseline composites. Therefore, an acoustic emissions (AE) based non-destructive testing (NDT) methodology was adopted here to assess and compare the damage propagation across both composite types [38], [62] - [64]. An AE sensor mounted in proximity to the sample was used to record energy dissipations in the form of temporal elastic waves, that are produced when the flexural specimens are subjected to internal damage. An illustration of the test set-up has been provided in Fig. S1.

Fig. 5 shows the mechanical, *in situ* acoustic and electrical responses (from CNTs) obtained from flexural testing of the composites. Under quasi-static loading conditions (Fig. 5a and Fig. 5b), the stress-strain curves of baseline (Ctrl) and CNT (Ctrl) composites show a similar near-linear response until failure, but the acoustic emissions from both composites illustrate notable differences in damage propagation. In the baseline composites, few, but large acoustic emissions that correspond to fiber damage or breakage occur mainly at high strain percentages, i.e., close to failure (Fig. 5a) [62]. In comparison, the CNT composites experience several low energy emissions pertaining to matrix micro-cracking that commence at strains close to 0.5 % (Fig. 5b) and span the entire testing period. The micro-crack growth is effectively retarded by the presence of the CNT

network (CNT bridging, CNT pull out), such that the strain energy is dissipated and the cracks are arrested. Further loading shifts the principle stress to another location and the micro-cracking process repeats itself until alumina fiber breakage leads to complete sample failure (as indicated by the increase in the AE events or steps). The micro-cracks and damage (as observed from the AE emissions) increase the electrical resistivity of the CNT composites by causing disruptions in the CNT network (as previously observed [62]). It is important to note that the CNT composites did not display measurable resistivity changes at smaller strains (lower than 0.5 %), as observed from a relatively flat initial section of the resistivity curves (Fig. 5b, Fig. 5d, and Fig. 5f). This may be a result of the strain heterogeneities introduced during the 3-point bend test or the lack of measurement sensitivity in the two-probe technique.

From Fig. 5c and 5d, it is evident that the failure mechanisms in both composites after Hy exposure remain similar to their respective control samples. As previously shown in Fig. 4a and Fig. 4b, the Hy samples underwent no major structural changes during their six-month exposure period. However, when the composites were subjected to hydrothermal conditions even for a relatively short time frame ≈ 15 d (HT-S) (Fig. 5e), there is a noticeable change in the failure mechanism of the baseline composites. Apart from lowered flexural strength and strain to failure, majority of these specimens do not exhibit any acoustic energy dissipations until failure. This behavior is attributed to poor load transferability between alumina fibers and the epoxy matrix caused by fiber/polymer degradation or interfacial delamination between the two components, that results in rapid crack growth and loss of structural properties [38].

The CNT composites display similar failure mechanisms before and after the hydrothermal exposure (Fig. 5b and 5f). As discussed previously, the CNT networks locally toughen the epoxy matrix and provide multiple, tortuous paths for crack propagation, which remain unaffected despite the aging environments [25]. The presence of multiple crack paths is further suggested by the gradual increase in electrical resistance (as a function of strain induced damage), which closely follows the acoustic energy emissions in all the exposure experiments (Figs. 5b, 5d and 5f). Thus, the multifunctional capabilities (structural and damage sensing) of the CNT composites remain intact, even after the environmental exposures.

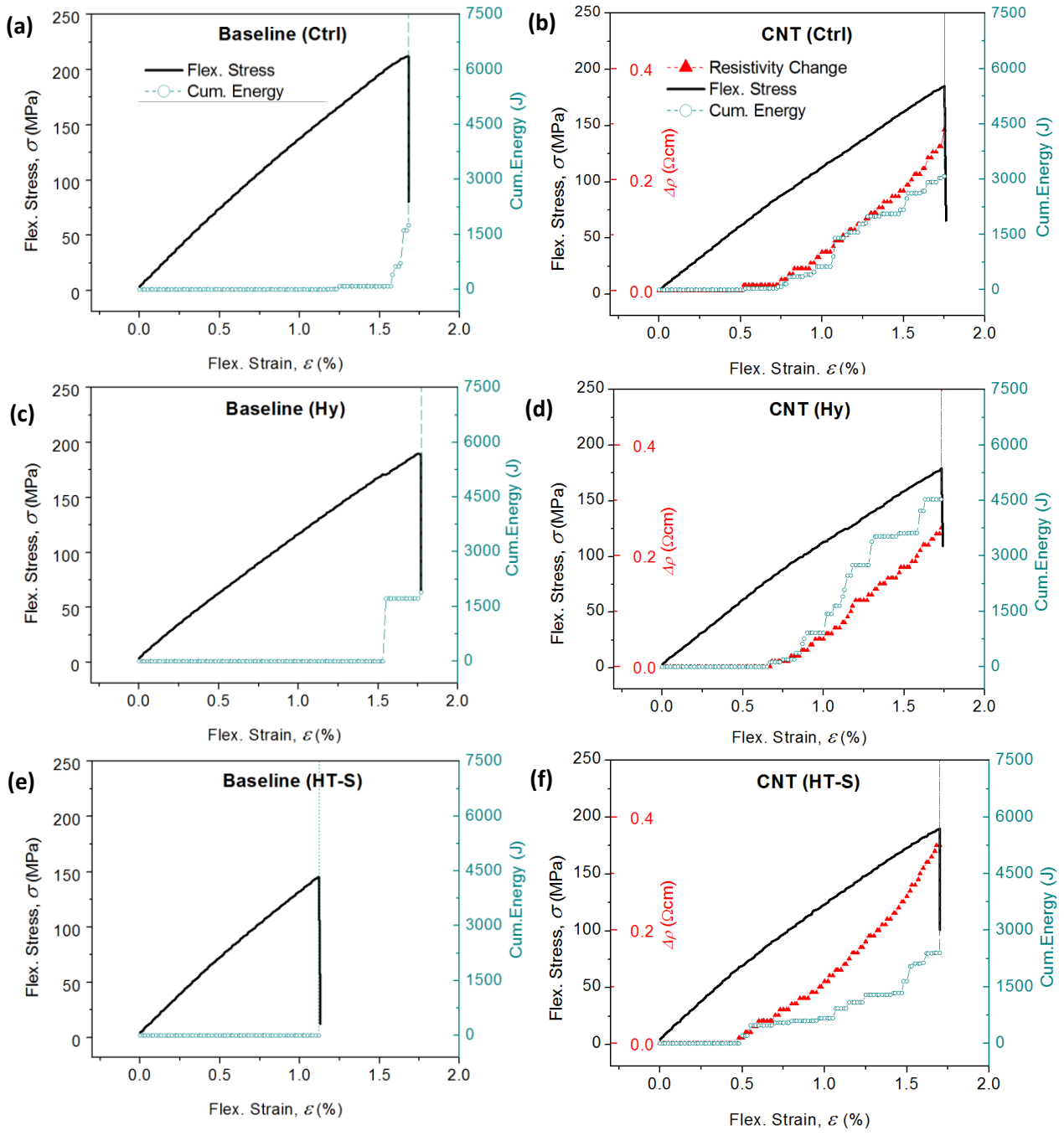

Figure 5: Flexural properties (Flex. Stress vs. Flex. Strain), *in situ* acoustic emissions (Cum. Energy vs. Flex. Strain) and electrical data (Resistivity change vs. Flex. Strain) for baseline and CNT composites at Ctrl, Hy (25 °C, 180 d), and HT-S (60 °C, 15 d) conditions. The acoustic and electrical properties are displayed only until failure to highlight the sensitivity of the characterization methods in detecting small scale damage propagation.

3.3.Fractography analysis:

The flexure samples were characterized using SEM imaging to corroborate the differences in failure characteristics before and after exposure to the aging environments. High-contrast, low-magnification SEM images presented in Fig. 6 (grayscale SEM images in Fig. S6) show crack propagation from the bottom to the top surface in all composites. This is typical of tensile surface failure in a bending geometry, initiated in the outer fiber plies due to large tensile forces originating from the loading conditions. Both the baseline and the CNT composites exhibit significant crack deflections and micro-cracking until failure at Ctrl and Hy conditions (Fig. 6b to Fig. 6e). The micro-cracks observed in the SEM images can be associated with low strain, acoustic energy emissions observed in the CNT specimens and high strain events in the case of the baseline specimens, as shown in Fig. 5a to Fig. 5d. After HT-S exposure, the baseline composites show reduced crack branching and near-linear, uninterrupted crack growth, which correlates with the loss of mechanical and acoustic properties in these specimens (Fig. 6f and Fig. 5e). In comparison, the damage propagation in the CNT composites remained similar across all exposure conditions, and is composed of multiple deflections and branching as shown in Figs. 6c, 6e and 6g.

The hackle patterns present on fiber and resin surfaces (Fig. 7a and Fig. 7b) indicate brittle fracture as the primary mode of failure in both baseline (Ctrl) and CNT (Ctrl) composites. These failure mechanisms appear to remain similar even after three months of hydrothermal aging (Fig. 7c and Fig. 7d). Thus, the lack of physical features indicating component degradation (fiber or polymer) suggests fiber/epoxy interfacial debonding as a possible explanation for strength reduction in the baseline composites.

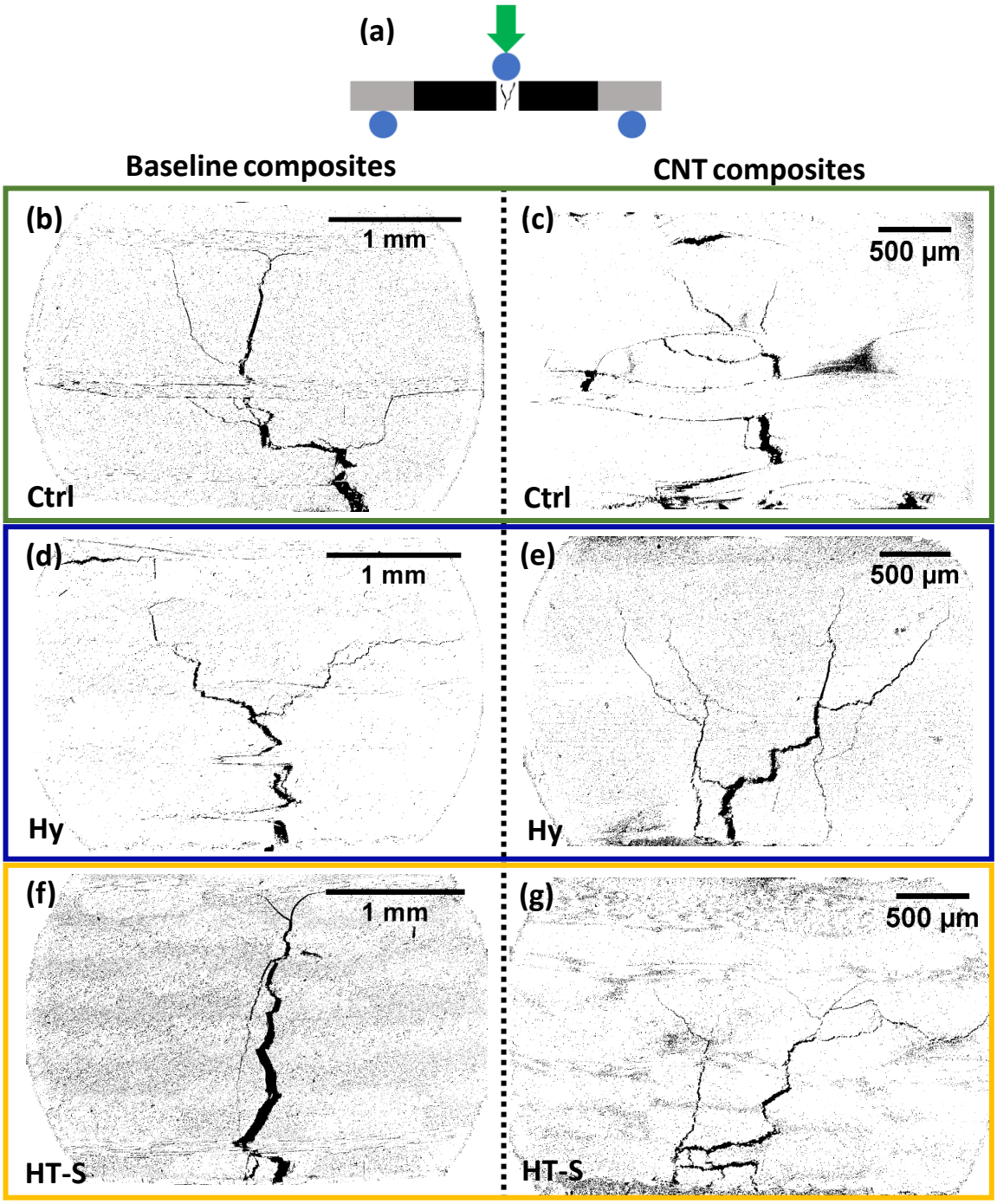

Figure 6: High-contrast, low-magnification SEM images of crack propagation on the side surfaces (a), in baseline and CNT flexure specimens after Ctrl, Hy (25 °C, 180 d), and HT-S (60 °C, 15 d) exposures (b) to (g). The top and bottom of each SEM image represents the top and the bottom loading surfaces of the composite specimens where the crack propagates from the bottom to the top surface upon failure.

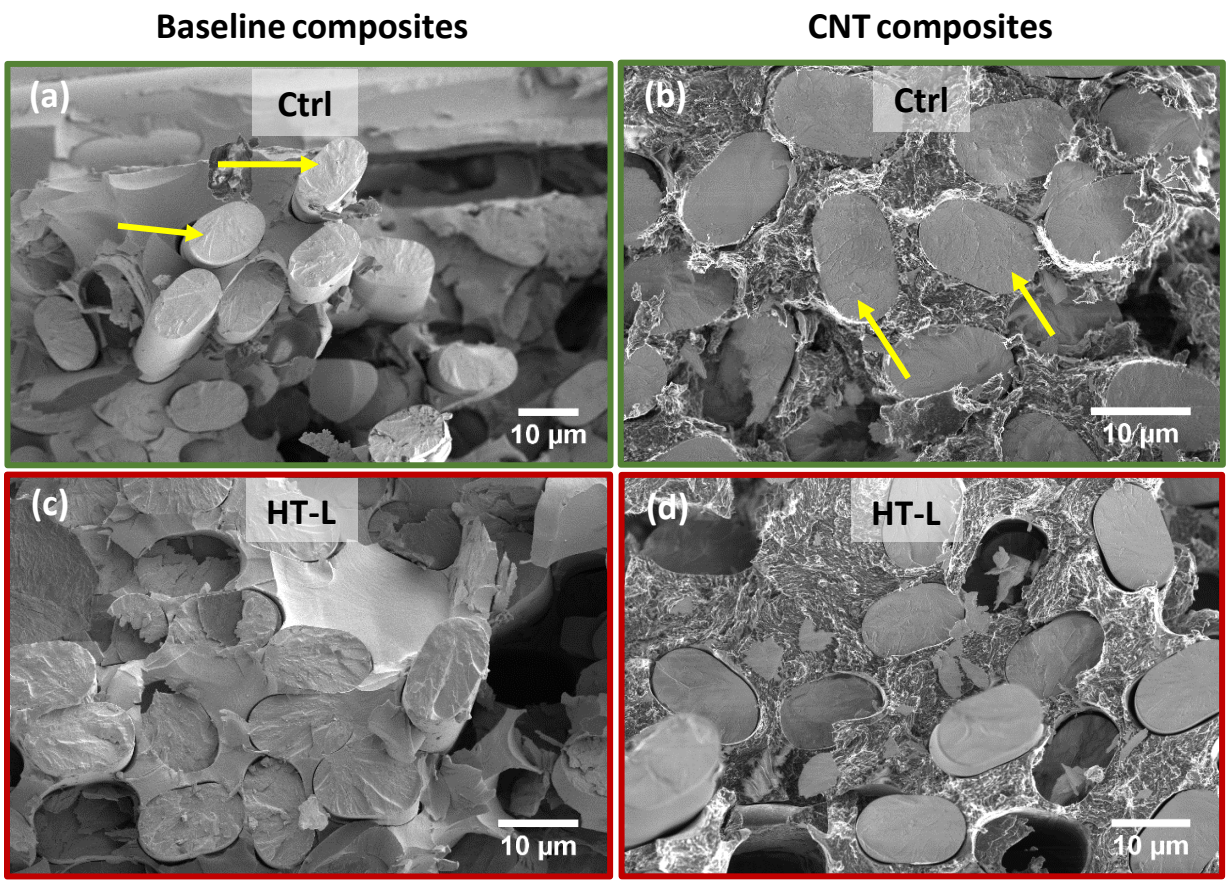

Figure 7: High-magnification, SEM images of failed composite cross-sections in flexure specimens after Ctrl and HT-L (60 °C, 90 d) exposures (region of interest shown in Fig. S3b). The yellow arrows point to the hackle patterns observable on fiber surfaces when the composites undergo brittle fracture.

3.4.Polymer Degradation

Polymer aging could manifest primarily through reduced flexural strength and mild surface discoloration as opposed to drastic changes in bending modulus in the hydrothermally treated baseline composites. Analytical measurements such as FTIR-ATR and DSC were used to confirm this. The resin used in the study, RTM6 epoxy, is a combination of tetraglycidylmethylenedianiline (TGMDA) resin and 4,4'-methylenebis-(2,6-diethylaniline) (MBDA)/4,4'-methylenebis-(2-isopropyl-6-methylaniline) (MBIMA) curing agents, as shown in Fig. S7. The averaged, mid-IR spectrum of the resin-rich region within the sectioned inner cross-sections is presented in Fig. S8. The effect of water on epoxy resins can be identified by two distinct peaks: ≈ 3600 cm^{-1} (mobile water) and ≈ 3300 cm^{-1} (resin bound water) [65]. Though, the hydroxyl peak at 3300 cm^{-1} overlaps

with the peak intensities of primary and secondary amines, the changes in the 3300 cm^{-1} to 3500 cm^{-1} region are often used to identify hydration reactions occurring within the resin [66] - [68].

From Fig. S8, the lack of changes in intensity at the 3600 cm^{-1} peak with increased exposure indicates the near absence of free water within the composites. On averaging the 3398 cm^{-1} peak intensity across normalized absorbance spectra, no significant peak shifts or intensity changes were observed within the region of importance (3300 cm^{-1} to 3500 cm^{-1}) (Fig. 8a). This confirms the absence of chemical changes in the bulk polymer resin after hydrothermal exposure.

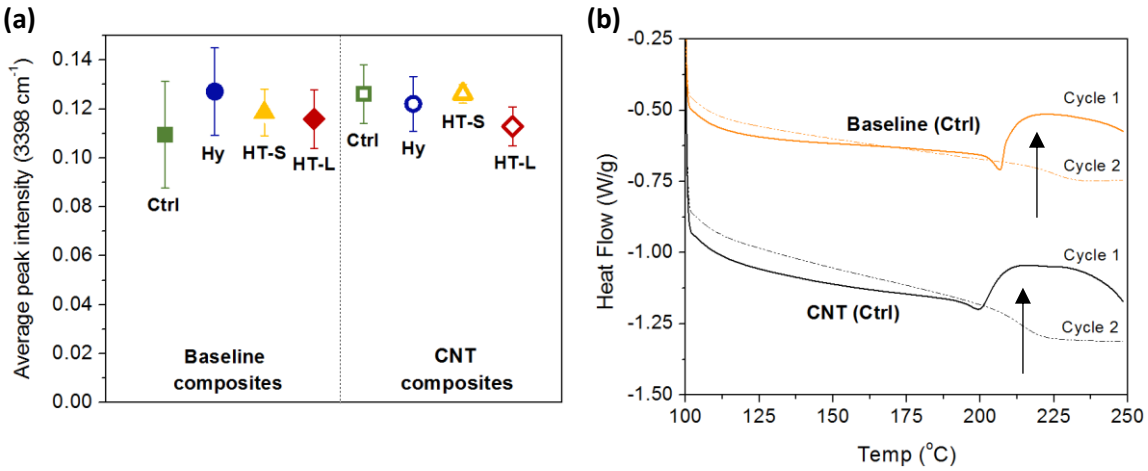

Figure 8: Polymer characterization using FTIR-ATR and DSC (region of interest shown in Fig. S3b). (a) Unchanged mean of the peak intensity at 3398 cm^{-1} denotes absence of resin hydrolysis. The uncertainties represent the standard deviation of the mean peak intensity calculated from 4 measurements at t_{max} for Ctrl, Hy (25 °C, 180 d), HT-S (60 °C, 15 d), and HT-L (60 °C, 90 d) exposures. (b) DSC measurements (heating cycles) of baseline (Ctrl) and CNT (Ctrl) composites. The solid and dashed lines indicate first and second heating cycles, respectively. The arrows indicate the broad exotherms corresponding to uncured epoxy observed during the first heating cycle.

The lack of irreversible chemical changes in the epoxy matrix was further confirmed by studying differences in thermal properties using DSC measurements. Fig. 8b shows the heat flow *versus* temperature for both heating cycles in the control specimens. In cycle 1, a broad exotherm appears above the glass transition region, which indicates the presence of unreacted epoxy in the composites [69]. This exotherm is replaced by a shift in the baseline (increase in T_g) during cycle 2. The increase in composite T_g signifies residual post-cure reactions that have occured within the

epoxy resin during the first heating cycle of DSC measurements, and are typical of composite specimens stored/operated at environmental conditions lower than their ultimate T_g [70]. Similar exotherms corresponding to unreacted epoxy were observed in cycle 1 for all the exposed specimens (Fig. S9), which suggests the absence of additional secondary cross-linking reactions between water and unreacted epoxides, often observed during long term hydrothermal experiments [43], [46].

The potential T_g depression caused by polymer chain scission was also evaluated. The T_g values of the exposed specimens remain unchanged within the uncertainties for the measurements conducted, indicating the absence of structurally compromised, low density polymer chains that form due to irreversible hydrolysis of the epoxy matrix (Table 4). Thus, by using a high T_g, hydrothermally stable aerospace resin, we eliminate matrix degradation as a possible cause of strength loss at these exposure conditions.

Table 4: T_g measurements of baseline and CNT composites determined using DSC (region of interest shown in Fig. S3b). The uncertainties represent the standard deviation of the mean T_g of 2 specimens at t_{max} for each condition.

Glass transition temperature, T_g (°C)		
Exposure condition	Baseline composite	CNT composite
Ctrl	201.45 ± 3.17	207.28 ± 0.81
Hy (25 °C, 180 d)	200.41 ± 2.14	208.23 ± 1.58
HT-S (60 °C, 15 d)	204.54 ± 0.95	207.75 ± 1.83
HT-L (60 °C, 90 d)	201.93 ± 2.72	208.29 ± 0.19

3.5.Alumina hydration and interfacial failure

Hydration of alumina surfaces is a phenomenon that is observed even at room temperature conditions [71]. At large concentrations of water or moisture, the defective sites on the amorphous alumina surfaces readily hydrolyze at low temperatures (0 °C to 100 °C) between a pH range of 5 to 7 to form bayerite crystals (β-$Al(OH)_3$) that are structurally weaker than alumina [72]. The reaction mechanism has been provided below (Eqn. 6 and 7) [73]. The water inclusions in the bayerite structure causes a 3x volumetric expansion on the oxide surface that result in a poor

adhesion between the hydroxides and the base oxide. This has previously been shown to cause interfacial delamination and loss of adhesion strength in the alumina/epoxy interface [74], [75].

$$Al_2O_3 + H_2O \rightarrow 2AlOOH \quad (6)$$

$$AlOOH + 2H_2O \rightarrow Al(OH)_3 \quad (7)$$

Though precipitates of alumina hydrolysis (bayerite and boehmite) were identified on the external fiber surfaces (direct water contact) of the exposed baseline and CNT composites (Figs. S10-S12), no evidence of these deposits were found on failed, internal cross-sections after the hydrothermal exposure, as previously shown using SEM (Fig. 7 and Fig. 9). The fibers embedded inside the polymer matrix are generally not susceptible to the large-scale hydrolysis reactions observed on the outer fiber tows because of reduced water concentrations inside the composite, and the rigid nature of polymer matrix that resists structural expansions. This eliminates fiber degradation as a probable cause of strength failure in these composites.

Prior work on the bonding strength between alumina and polymer adhesives indicate that chemical changes in the alumina microstructure can affect the bond strength between the polymer and the metal oxide surface adversely [75] - [78]. Furthermore, CNT growth at high temperature conditions prevents the use of adhesion promoters (such as siloxanes) that can facilitate strong chemical bonds at the fiber/polymer interface. In the absence of primary chemical bonds, the interfacial strength between the alumina fiber surface and the epoxy is often limited to secondary van der Waals forces. These forces are not sufficient to prevent the ingress of water molecules, which then form hydrogen bonds between the fiber surface and the epoxy. Hence, the loss of strength is attributed to the disruption of primary and secondary bonds between the fiber and the polymer surfaces, caused by diffusion of water to the interfacial regions of the composite [79], [80]. As previously shown by Kinloch et al. [80], the work of adhesion (energy required to separate unit area of two phases) for an epoxide/Al_2O_3 joint reduces from 232 mJ/m^2 in dry environments to -137 mJ/m^2 in the presence of water. The result is the formation of a thin water layer that can sufficiently separate the two interacting surfaces to induce poor load transferability within the composite structure.

Although the kinetics of interface degradation is beyond the scope of the current study, it is evident that this reaction is highly favorable at high-temperature, hydrothermal conditions (60 °C), where

the mechanical properties of the baseline composites deteriorate rapidly. We hypothesize that at high temperatures, water diffusion leads to extensive disruption of the van der Waals bonding at the fiber/polymer interface [81], which leads to immediate deterioration in the strength properties of the baseline composites. The ability of water to reduce bond strength at the fiber matrix interface has been shown for pultruded glass fiber reinforced polymers, but unlike that study we were not able to discern any changes in the fracture properties of the aluminoborosilicate fibers at failure [2], [81]. However, in the presence of interconnected, MWCNT networks at the fiber/polymer interfaces, secondary toughening mechanisms manifest in the form of microcracking caused by CNT fiber pullouts and CNT fractures, that preserve the structural properties of the CNT composites (Fig. 10). This prevents onset of early sample failure and prolongs the operation cycle of these multifunctional composites.

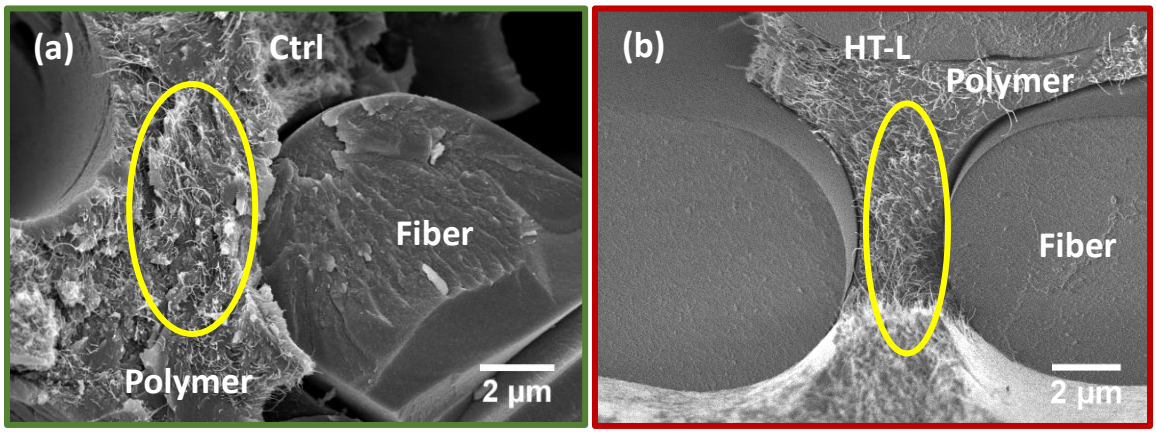

Figure 9: High-magnification, SEM images of failed CNT composite cross-sections in flexure specimens after (a) Ctrl, and (b) HT-L (60 °C, 90 d) exposures (region of interest shown in Fig. S3b). The highlighted sections show the dominance of CNT pullouts and CNT fractures due to the secondary reinforcement mechanisms observed in CNT composites. These reinforcements remain intact even after the long-term hydrothermal exposure.

4. Conclusions

The increasing demand for commercialization of CNT reinforced fiber composites makes it important to understand their degradation characteristics under environments that induce aging. With no prior study on the effects of aging environment on the interfacial properties of CNT reinforced fiber composites, this work examines the durability of nanoengineered hierarchical

CNT composites, and identifies a specific interfacial degradation route. We show that the presence of CVD-grown, radially-aligned CNT networks at the fiber/polymer interface enhances the durability of these nanocomposites under hydrothermal and hydro conditions, even at long exposure periods (three months and six months). Water permeability in the CNT composites was found to be marginally lower than the baseline composites due to the presence of dense CNT networks that provide a circuitous path for the transport of water (as previously observed) [43], [44]. However, the presence of CNTs was not found to affect the equilibrium water content or the activation barrier for diffusion in these systems. The absence of interfacial chemical bonding in the form of organic sizing agents (such as siloxanes) between the fiber and the polymer, allows water molecules to disrupt and separate the weak fiber/polymer interfaces at high temperatures, that led to a massive loss of strength in the baseline composites, even at short exposure durations. However, in the CNT composites, damage propagation is hindered by the presence of strong CNT/polymer interfaces that provide secondary reinforcement mechanisms in the form of crack deflection, CNT pullouts and CNT fractures, which allow CNT specimens to preserve their multifunctional properties (structural and electrical) even under accelerated aging environments. The results of this fiber composite system provide a new understanding of these materials and their structure-process-property relationships, which can be extended to other commercially viable fiber/matrix systems. This comprehensive knowledge is essential to accelerate materials innovation by coupling experimental aging data to more rapidly develop new multi length-scale and multi physics models, as per the vision of Materials Genome Initiative (MGI) [82].

Acknowledgements

Research conducted by A. Krishnamurthy was performed under financial assistance award (Grant #70NANB15H272) from the U.S. Department of Commerce, National Institute of Standards and Technology. B. Natarajan acknowledges the support of the Air Force Office of Scientific Research (Award No. F1ATA00236G002). The work at MIT was supported by Airbus, Boeing, Embraer, Lockheed Martin, Saab AB, ANSYS Inc., and TohoTenax through MIT's Nano-Engineered Composite aerospace STructures (NECST) Consortium. S.S. Wicks was supported by the NASA Space Technology Research Fellowships (NSTRF) and MIT's Linda and Richard (1958) Hardy Fellowship.

References

[1] Bakis C, Bank L, Brown V, Cosenza E, Davalos J, Lesko J, Machida A, Rizkalla S, Triantafillou T. Fiber-reinforced polymer composites for construction-state-of-the-art review. J Comp Constr 2002;6:73–87.

[2] Liao K, Schultheisz CR, Hunston DL, Brinson LC. Long-term durability of fiber-reinforced polymer-matrix composite materials for infrastructure applications: A review. J Adv Mater 1998;30:3–40.

[3] Cantwell WJ, Morton J. The impact resistance of composite materials - a review. Composites 1991;22:347–62. doi:10.1016/0010-4361(91)90549-V.

[4] Zhao XL, Zhang L. State-of-the-art review on FRP strengthened steel structures. Eng Struct 2007;29:1808–23. doi:10.1016/j.engstruct.2006.10.006.

[5] Veedu VP, Cao A, Li X, Ma K, Soldano C, Kar S, et al. Multifunctional composites using reinforced laminae with carbon-nanotube forests. Nat Mater 2006;5:457–62. doi:10.1038/nmat1650.

[6] Kyriakides S, Arseculeratne R, Perry EJ, Liechti KM. On the compressive failure of fiber reinforced composites. Int J Solids Struct 1995;32:689–738. doi:10.1016/0020-7683(94)00157-R.

[7] Mouritz AP, Bannister MK, Falzon PJ, Leong KH. Review of applications for advanced three-dimensional fibre textile composites. Compos Part A Appl Sci Manuf 1999;30:1445–61. doi:10.1016/S1359-835X(99)00034-2.

[8] Mouritz AP, Cox BN. A mechanistic interpretation of the comparative in-plane mechanical properties of 3D woven, stitched and pinned composites. Compos Part A Appl Sci Manuf 2010;41:709–28. doi:10.1016/j.compositesa.2010.02.001.

[9] Gojny FH, Wichmann MHG, Fiedler B, Bauhofer W, Schulte K. Influence of nano-modification on the mechanical and electrical properties of conventional fibre-reinforced composites. Compos Part A Appl Sci Manuf 2005;36:1525–35. doi:10.1016/j.compositesa.2005.02.007.

[10] Allaoui A, Bai S, Cheng HM, Bai JB. Mechanical and electrical properties of a MWNT/epoxy composite. Compos Sci Technol 2002;62:1993–8. doi:10.1016/S0266-3538(02)00129-X.

[11] Gohardani O, Elola MC, Elizetxea C. Potential and prospective implementation of carbon nanotubes on next generation aircraft and space vehicles: A review of current and expected applications in aerospace sciences. Prog Aerosp Sci 2014;70:42–68. doi:10.1016/j.paerosci.2014.05.002.

[12] Bekyarova E, Bekyarova E, Thostenson ET, Thostenson ET, Yu a, Yu a, et al. Multiscale carbon nanotube-carbon fiber reinforcement for advanced epoxy composites. Langmuir 2007;23:3970–4. doi:10.1021/la062743p.

[13] Thostenson ET, Li C, Chou TW. Nanocomposites in context. Compos Sci Technol 2005;65:491–516. doi:10.1016/j.compscitech.2004.11.003.

[14] Pukánszky B. Influence of interface interaction on the ultimate tensile properties of polymer composites. Composites 1990;21:255–62. doi:10.1016/0010-4361(90)90240-W.

[15] Yeh MK, Hsieh TH, Tai NH. Fabrication and mechanical properties of multi-walled carbon nanotubes/epoxy nanocomposites. Mater Sci Eng A 2008;483-484:289–92. doi:10.1016/j.msea.2006.09.138.

[16] Ma PC, Mo SY, Tang BZ, Kim JK. Dispersion, interfacial interaction and re-agglomeration of functionalized carbon nanotubes in epoxy composites. Carbon N Y 2010;48:1824–34. doi:10.1016/j.carbon.2010.01.028.

[17] Schadler LS, Kumar SK, Benicewicz BC, Lewis SL, Harton SE. Designed interfaces in polymer composites: a fundamental viewpoint. MRS Bull 2007;32:335–40.

[18] Song YS, Youn JR. Influence of dispersion states of carbon nanotubes on physical properties of epoxy nanocomposites. Carbon N Y 2005;43:1378–85. doi:10.1016/j.carbon.2005.01.007.

[19] Shi DL, Feng XQ, Huang YY, Hwang KC, Gao H. The Effect of Nanotube Waviness and Agglomeration on the Elastic Property of Carbon Nanotube-Reinforced Composites. J Eng Mater Technol 2004;126:250. doi:10.1115/1.1751182.

[20] Fiedler B, Gojny FH, Wichmann MHG, Nolte MCM, Schulte K. Fundamental aspects of nano-reinforced composites. Compos Sci Technol 2006;66:3115–25. doi:10.1016/j.compscitech.2005.01.014.

[21] Wicks SS, de Villoria RG, Wardle BL. Interlaminar and intralaminar reinforcement of composite laminates with aligned carbon nanotubes. Compos Sci Technol 2010;70:20–8. doi:10.1016/j.compscitech.2009.09.001.

[22] García EJ, Hart AJ, Wardle BL, Slocum AH. Fabrication of composite microstructures by capillarity-driven wetting of aligned carbon nanotubes with polymers. Nanotechnology 2007;18:165602. doi:10.1088/0957-4484/18/16/165602.

[23] Liotta AH, Wicks SS, Wardle BL, Lomov SV. Internal geometry of woven composite laminates with " fuzzy " carbon nanotube grafted fibers. Compos Part A 2016;88:295–304. doi:10.1016/j.compositesa.2016.06.010.

[24] Garcia EJ, Wardle BL, Hart AJ, Yamamoto N. Fabrication and multifunctional properties of a hybrid laminate with aligned carbon nanotubes grown In Situ. Compos Sci Technol 2008;68:2034–41. doi:10.1016/j.compscitech.2008.02.028.

[25] Wicks SS, Wang W, Williams MR, Wardle BL. Multi-scale interlaminar fracture mechanisms in woven composite laminates reinforced with aligned carbon nanotubes. Compos Sci Technol 2014;100:128–35. doi:10.1016/j.compscitech.2014.06.003.

[26] Lachman N, Wiesel E, Guzman de Villoria R, Wardle BL, Wagner HD. Interfacial load transfer in carbon nanotube/ceramic microfiber hybrid polymer composites. Compos Sci Technol 2012;72:1416–22. doi:10.1016/j.compscitech.2012.05.015.

[27] Shah TK, Malecki HC, Adcock DJ. CNT-based resistive heating for deicing composite structures. US 8,664,573 B2, 2014.

[28] Yamamoto N, Guzman de Villoria R, Wardle BL. Electrical and thermal property enhancement of fiber-reinforced polymer laminate composites through controlled

implementation of multi-walled carbon nanotubes. Compos Sci Technol 2012;72:2009–15. doi:10.1016/j.compscitech.2012.09.006.

[29] UTC Aerospace Systems. Tiny technology. Big breakthrough. UTC Aerospace Systems is changing the industry with its lightest ice protection systems ever 2017:1. http://news.utcaerospacesystems.com/2017-01-19-Tiny-technology-Big-breakthrough-UTC-Aerospace-Systems-is-changing-the-industry-with-its-lightest-ice-protection-systems-ever.

[30] Collins D, Freels J. Accelerated Test Methods for Reliability Prediction. J Qual Technol 2013;45:244–59.

[31] Gullo LJ. Highly Accelerated Life Testing. In: Design for Reliability, editors. Raheja D, Gullo LJ., Hoboken, NJ: John Wiley & Sons, Inc.; 2012, p. 169–81. doi:10.1002/9781118310052.ch11.

[32] Costa ML, Rezende M., De Almeida SFM. Strength of Hydrothermally Conditioned Polymer Composites with Voids. J Compos Mater 2005;39:1943–61. doi:10.1177/0021998305051807.

[33] Surathi P, Karbhari VM. Hydrothermal effects on durability and moisture kinetics of fiber-reinforced. San Diego: 2006.

[34] Akay M, Ah Mun SK, Stanley A. Influence of moisture on the thermal and mechanical properties of autoclaved and oven-cured Kevlar-49/epoxy laminates. Compos Sci Technol 1997;57:565–71. doi:http://dx.doi.org/10.1016/S0266-3538(97)00017-1.

[35] Gaur U, Miller B. Effects of Environmental Exposure on Fiber/Epoxy Interfacial Shear Strength. Polymer (Guildf) 1990;11:217–22.

[36] Halpin J. Effects of Environmental Factors on Composite Materials. 1969.

[37] Liao K, Schultheisz CR, Hunston DL. Long-term environmental fatigue of pultruded glass-fiber-reinforced composites under flexural loading. Int J Fatigue 2000;21:485–95. doi:10.1016/S0142-1123(98)00088-7.

[38] Sekine H, Shimomura K, Hamana N. Strength Deterioration and Degradation Mechanism of Glass Chopped Reinforced Plastics in Water Environment. JSME Int J 1988;31:619–25.

[39] Fazal A, Fancey KS. Performance enhancement of nylon kevlar fiber composites through viscoelastically generated pre-stress. Polym Polym Compos 2008;16:101–13. doi:10.1002/pc.

[40] Chateauminois A, Vincent L. Hydrothermal Ageing Effects on the Static Fatigue Behaviour of a Glass Epoxy. Composite Damage Mechanisms Mapping. Oil Gas Sci Technol 1995;50:97–104. doi:10.2516/ogst:1995010.

[41] Zaman A, Gutub SA, Wafa MA. A review on FRP composites applications and durability concerns in the construction sector. J Reinf Plast Compos 2013;32:1966–88. doi:10.1177/0731684413492868.

[42] Karbhari VM. Durability of composites for civil structural applications. Elsevier; 2007.

[43] Prolongo SG, Gude MR, Ureña A. Water uptake of epoxy composites reinforced with carbon nanofillers. Compos Part A Appl Sci Manuf 2012;43:2169–75. doi:10.1016/j.compositesa.2012.07.014.

[44] Starkova O, Buschhorn ST, Mannov E, Schulte K, Aniskevich A. Water transport in epoxy/MWCNT composites. Eur Polym J 2013;49:2138–48. doi:10.1016/j.eurpolymj.2013.05.010.

[45] Starkova O, Chandrasekaran S, Prado LASA, Tölle F, Mülhaupt R, Schulte K. Hydrothermally resistant thermally reduced graphene oxide and multi-wall carbon nanotube based epoxy nanocomposites. Polym Degrad Stab 2013;98:519–26. doi:10.1016/j.polymdegradstab.2012.12.005.

[46] Bal S, Saha S. Effect of sea and distilled water conditioning on the overall mechanical properties of carbon nanotube/epoxy composites. Int J Damage Mech 2015;0:1–13. doi:10.1177/1056789515615184.

[47] Garg M, Sharma S, Mehta R. Carbon nanotube-reinforced glass fiber epoxy composite laminates exposed to hydrothermal conditioning. J Mater Sci 2016;51:8562–78. doi:10.1007/s10853-016-0117-z.

[48] Qian H, Greenhalgh ES, Shaffer MSP, Bismarck A. Carbon nanotube-based hierarchical composites: a review. J Mater Chem 2010;20:4751. doi:10.1039/c000041h.

[49] Li R, Lachman N, Florin P, Wagner HD, Wardle BL. Hierarchical carbon nanotube carbon fiber unidirectional composites with preserved tensile and interfacial properties. Compos Sci Technol 2015;117:139–45. doi:10.1016/j.compscitech.2015.04.014.

[50] Lomov S V, Wicks S, Gorbatikh L, Verpoest I, Wardle B. Compressibility of nanofibre-grafted alumina fabric and yarns: Aligned carbon nanotube forests. Compos Sci Technol 2014;90:57–66. doi:http://dx.doi.org/10.1016/j.compscitech.2013.10.017.

[51] Wicks S, Ishiguro K, Guzman de Villoria R, Wardle B. Mechanical Properties of Infusion-Processed Fiber Reinforced Plastics with In Situ-Grown Aligned Carbon Nanotubes. 51st AIAA/ASME/ASCE/AHS/ASC Struct. Struct. Dyn. Mater. Conf. 18th AIAA/ASME/AHS Adapt. Struct. Conf. 12th, 2010, p. 1–9. doi:10.2514/6.2010-2569.

[52] ASTM Standard D 790. Standard Test Method for Flexural Properties of Polymer Matrix Composite Materials. American Society for Testing and Materials, West Conshohocken, PA. 2015.

[53] ASTM Standard E 976. Standard Guide for Determining the Reproducibility of Acoustic Emission Sensor Response. American Society for Testing and Materials, West Conshohocken, PA. 2005.

[54] Perret B, Schartel B, StoB K, Ciesielski M, Diederichs J, Doring M, et al. Novel DOPO-based flame retardants in high-performance carbon fibre epoxy composites for aviation. Eur Polym J 2011;47:1081–9. doi:10.1016/j.eurpolymj.2011.02.008.

[55] Schindelin J, Rueden CT, Hiner MC, Eliceiri KW. The ImageJ ecosystem: An open platform for biomedical image analysis. Mol Reprod Dev 2015;82:518–529. doi:10.1002/mrd.22489.

[56] Simar A., Gigliotti M, Grandidier JC, Ammar-Khodja I. Evidence of thermo-oxidation phenomena occurring during hydrothermal aging of thermosetting resins for RTM composite applications. Compos Part A Appl Sci Manuf 2014;66:175–82. doi:10.1016/j.compositesa.2014.07.007.

[57] Bonniau P, Bunsell AR, Materiaux C, Mines E. A Comparative Study of Water Absorption Theories Applied to Glass Epoxy Composites. J Compos Mater 1981;15:0272–22.

[58] Guadagno L, Vertuccio L, Sorrentino A, Raimondo M, Naddeo C, Vittoria V, et al. Mechanical and barrier properties of epoxy resin filled with multi-walled carbon nanotubes. Carbon N Y 2009;47:2419–30. doi:10.1016/j.carbon.2009.04.035.

[59] ASTM Standard D 2344. Standard Test Method for Short-Beam Strength of Polymer Matrix Composite Materials and Their Laminates. American Society for Testing and Materials, West Conshohocken, PA. 2016.

[60] Cotronics Corporation. Ultra temp. tape and cloth. http://www.cotronics.com/vo/cotr/pdf/391.pdf.

[61] Thostenson ET, Chou TW. Carbon nanotube networks: Sensing of distributed strain and damage for life prediction and self healing. Adv Mater 2006;18:2837–41. doi:10.1002/adma.200600977.

[62] Gao L, Thostenson ET, Zhang Z, Chou TW. Coupled carbon nanotube network and acoustic emission monitoring for sensing of damage development in composites. Carbon N Y 2009;47:1381–8. doi:10.1016/j.carbon.2009.01.030.

[63] Liu PF, Chu JK, Liu YL, Zheng JY. A study on the failure mechanisms of carbon fiber/epoxy composite laminates using acoustic emission. Mater Des 2012;37:228–35. doi:10.1016/j.matdes.2011.12.015.

[64] Bourchak M, Khan A. Acoustic Emission Characterization of Matrix Damage Initiation in Woven CFRP Composites. Mater Sci Appl 2013;4:509–15.

[65] González-González M, Cabanelas JC, Baselga J. Applications of FTIR on Epoxy Resins - Identification, Monitoring the Curing Process, Phase Separation and Water Uptake. In: Theophile T, editor. Infrared Spectrosc. - Mater. Sci. Eng. Technol., vol. 2, Madrid: InTech; 2012, p. 261–84. doi:10.5772/36323.

[66] Lin YC, Chen X, Zhang HJ, Wang ZP. Effects of hydrothermal aging on epoxy-based anisotropic conductive film. Mater Lett 2006;60:2958–63. doi:10.1016/j.matlet.2006.02.024.

[67] Xiao GZ, Delamar M, Shanahan MER. Irreversible interactions between water and DGEBA/DDA epoxy resin during hydrothermal aging. J Appl Polym Sci 1997;65:449–58. doi:10.1002/(SICI)1097-4628(19970718)65:3<449::AID-APP4>3.0.CO;2-H.

[68] Guo C, Zhou L, Lv J. Effects of expandable graphite and modified ammonium polyphosphate on the flame-retardant and mechanical properties of wood flour-polypropylene composites. Polym Polym Compos 2013;21:449–56. doi:10.1002/app.

[69] Miller SG, Roberts GD, Copa CC, Bail JL, Kohlman LW, Binienda WK. Effects of Hydrothermal Cycling on the Chemical , Thermal , and Mechanical Properties of 862 / W Epoxy Resin. Cleveland: 2011.

[70] Maurer JJ, Eustace DJ, Ratcliffe CT. Thermal characterization of poly(acrylic acid). Macromolecules 1987;20:196–202. doi:10.1021/jp204957k.

[71] Gates RS, Hsu M, Klaus EE. Tribochemical Mechanism of Alumina With Water. Tribol Trans 1989;32:357–63. doi:10.1080/10402008908981900.

[72] Wefers K, Misra C. Oxides and Hydroxides of Aluminum. Alcoa Tech Pap 1987;19:100.

[73] Johnson BB. Adhesive bonding of aluminium. Norwegian University of Science and Technology, 2003.

[74] Kinloch AJ, Welch LS, Bishop HE. The Locus of Environmental Crack Growth in Bonded Aluminium Alloy Joints. J Adhes 1984;16:165–77. doi:10.1080/00218468408074915.

[75] Adams DO, DeVries KL, Child C. Durability of Adhesively Bonded Joints For Aircraft Structures. FAA Jt Adv Mater Struct Cent Excell Tech Rev Meet 2012:22.

[76] Venables JD. Adhesion and durability of metal-polymer bonds. J Mater Sci 1984;19:2431–53. doi:10.1007/BF00550796.

[77] Lunder O. Chromate-free pre-treatment of aluminium for adhesive bonding. Norwegian University of Science and Technology, 2003.

[78] Davis GD. Durability of Adhesive Joints. Handb Adhes Technol 2003:273. doi:10.1002/sia.740170726.

[79] Gledhill RA, Kinloch AJ. Environmental Failure of Structural Adhesive Joints. J Adhes 1974;6:315–30. doi:10.1080/00218467408075035.

[80] Kinloch AJ. Adhesion and Adhesives: Science and Technology. Springer; 1987.

[81] Schmidt RG, Bell JP. Epoxy Adhesion to Metals. Adv Polym Sci 1986;75:33–71. doi:10.1007/BFb0017914.

[82] White A. The Materials Genome Initiative: One year on. MRS Bull 2012;37:715–6. doi:10.1557/mrs.2012.194.